Available online at www.sciencedirect.com
SCIENCE DIRECT
Cement and Concrete Research 35 (2005) 1665–1675
Cement and Concrete Research

Incorporation of zinc into calcium silicate hydrates, Part I: formation of C-S-H(I) with C/S=2/3 and its isochemical counterpart gyrolite

Andreas Stumm[a,*], Krassimir Garbev[a], Günter Beuchle[a], Leon Black[a,b], Peter Stemmermann[a], Rolf Nüesch[a]

[a]Forschungszentrum Karlsruhe GmbH, Hermann-von-Helmholtz-Platz 1, 76344 Eggenstein-Leopoldshafen, Germany
[b]Materials Research Institute, Sheffield Hallam University, Sheffield S1 1WB, England

Received 5 July 2004; accepted 15 November 2004

Abstract

We have investigated the incorporation of zinc into both nanocrystalline and crystalline calcium silicate hydrates with starting C/S ratios of 2/3 (0.66). Zinc was added replacing calcium in the starting mixtures [Zn/(Zn+Ca)=0–1/4; 0–10 wt.% Zn], and the resultant phases were characterised using X-ray diffraction (XRD), X-ray photoelectron spectroscopy (XPS), differential thermal analysis–thermogravimetry (DTA–TG) and environmental scanning electron microscopy (ESEM).

In both groups of samples, increasing zinc content led to gradual structural changes, until eventually a second phase was formed. Zinc was incorporated to similar limits in both sets of samples. The thermal stability of the structures increased to a certain zinc content, beyond which there was structural destabilisation. Zinc incorporation is possible up to ~6 wt.%. Our observations strongly indicate similar zinc incorporation mechanisms in both sample series, namely incorporation of zinc into the interlayer of C-S-H(I) and the X-sheet of gyrolite for nanocrystalline and crystalline samples, respectively.

Keywords: Calcium silicate hydrate (C-S-H); Zinc; Amorphous material; Crystal structure; Thermal treatment

1. Introduction

Waste solidification/stabilisation (S/S) often utilizes heavy metal fixation in cement paste [1]. Hardened Portland cement paste is an excellent storage material of heavy metals under short- and medium-term conditions.

Calcium silicate hydrates (C-S-H: where C=CaO; S=SiO_2; H=H_2O) in hardened cement pastes display approximate C/S ratios of 5/3, but can vary over the range 3/5–2 [2] depending upon hydration time, alteration and weathering. The incorporation of heavy metals into calcium silicate hydrates is important for their potential long-term immobilisation in hardened cement pastes.

In addition to S/S, heavy metals may also be present in cement clinkers, arising primarily via cocombustion of waste material in cement manufacture. The three most predominant heavy metals fixed within the structures of the clinker minerals are as follows: vanadium, present in large amounts in coal and petcoke; zinc, a minor element in tyres and other rubber materials and also in kiln dust; and lead, a trace element in raw materials [3,4].

The type of fixation of heavy metals in cement pastes, whether incorporation, sorption, or coprecipitation, is of major importance for safety assessment of these materials and their potential for recycling. In particular, the fate of contaminants during the weathering of cement matrices is unknown. Whilst the structure and behaviour of the basic materials (e.g. clinker phases) and some hydration products (e.g. aluminate hydrates, carbonates and hydroxides) are mostly known [5], the structure and the weathering behaviour of C-S-Hs are widely unknown. What is known is that weathering leads to loss of Ca, therefore phases with low C/S ratios, 0.5<C/S<1.0, must be assessed.

* Corresponding author. Tel.: +49 7247 82 6878.
E-mail address: andreas.stumm@itc-wgt.fzk.de (A. Stumm).

0008-8846/$ - see front matter © 2004 Elsevier Ltd. All rights reserved.
doi:10.1016/j.cemconres.2004.11.007

Zn is one of the most common heavy metals in cement pastes. It may be present in clinker, incorporated into C_3S [6] and MgO [3] or as $Ca_6Al_4Zn_3O_{15}$ [4]. Up to 4 wt.% zinc can be incorporated into the crystal lattice of synthetic C_3S [7]. Zinc may also arise in cement pastes via the oxidation of galvanic zinc coatings on steel. Its incorporation may also arise due to the addition of soluble Zn salts [8]. It is generally believed that zinc retards cement hydration via the formation of a layer of amorphous $Zn(OH)_2$ or crystalline $Ca[Zn(OH)_3 \cdot H_2O]_2$ around the anhydrous grains at the onset of hydration [9,10]. As calcium zincate disappears during the course of cement hydration, some authors believed that Zn is further fixed into portlandite [11]. However, more recently the role of C-S-H gel as a most probable fixing medium was increasingly recognized [12–14]. In particular, the incorporation of Zn^{2+} in the interlayer of C-S-H(I) or sorption onto internal crystallite surfaces appear to be the most probable mechanisms for C-S-H(I) [14].

In our study, which is part of larger project investigating incorporation of heavy metals in C-S-H phases, we have studied the incorporation of Zn into nanocrystalline C-S-H(I) with C/S=2/3 and its crystalline counterpart gyrolite: $Ca_{16}Si_{24}O_{60}(OH)_8 \cdot 14H_2O$. We regard this low C/S ratio as a representative example of an aged C-S-H gel, which may be formed in the course of weathering. Additionally the choice of gyrolite for our study was based upon three reasons. (1) Gyrolite can occur in some hydrated cements, especially those cured at high temperatures such as in deep oil wells, in aerated concrete or around cementitous stabilized nuclear waste [15,16]. (2) Studies of calcium silicate hydrate gels are difficult, because these materials are nearly amorphous [17]. However, crystalline C-S-H phases exist over the same range of C/S ratios. Their structures are generally known and thus they may be used as model substances in such investigations. (3) A comparative study such as this is of importance in revealing, not only the Zn-sorption potential of the C-S-H gel with C/S=2/3, but also that of its isochemical crystalline analogue gyrolite, which is completely unknown.

Because of the limitations of X-ray diffraction (XRD) in studying nanocrystalline phases, we have also applied techniques such as differential thermal analysis–thermogravimetry (DTA–TG) and X-ray photoelectron spectroscopy (XPS), which should make comparative investigations of crystalline phases (gyrolite) and their nanocrystalline precursors possible.

1.1. Structure and stability of C-S-H gel and gyrolite

Extensive studies have been made to elucidate the structure of the C-S-H phases. X-ray diffraction is of limited value since the phases are nearly amorphous, although the C-S-H phases show some reflections in their diffraction patterns which may be assigned mainly to ordering in the *xy* plane. A special case, showing additionally some ordering in the *z* direction, is C-S-H(I), which shows a basal reflection in the range 14–11 Å and in most of its features resembles the pattern of tobermorite. The position of the basal reflection seems to depend upon C/S and water/solid, w/s, ratios [18]. Because of the three-dimensional structural ordering of C-S-H(I), it is often referred to as nanocrystalline, a term we use further in this paper.

Many structural studies have been performed with methods not dependent upon long-range structural order, such as trimethylsilylation (TMS) [19], ^{29}Si MAS NMR [20-22], and vibrational spectroscopy [23,24]. A lot of structural models for C-S-H gel have been proposed, based upon these investigations, mostly incorporating the binary solid–solution mechanism. Both Fujii und Kondo [25] and Cong and Kirkpatrick [26] consider C-S-H gel as a solid solution of tobermorite and $Ca(OH)_2$, the so-called defect-tobermorite model, whilst Richardson and Groves [27] proposed model based on isolated silicate chains of variable length and OH content, intergrown with $Ca(OH)_2$. A widely known model is that proposed by Taylor [28,29], assuming that C-S-H gel consists of a mixture of 14 Å tobermorite and jennite domains on the nanometer scale.

Some authors propose that gyrolite formation takes place via a gyrolite gel phase [30]. This gel transforms firstly to Z phase (with a characteristic reflection at 15 Å in the powder diffraction pattern) from which gyrolite subsequently forms [31,32]. Gyrolite and tobermorite gel consist of single chains of silicate tetrahedra which are stacked turbostratically along the *c*-axis. Some authors propose that the *ab* plane is relatively well-ordered, having hexagonal or orthorhombic symmetry in gyrolite gel and tobermorite gel, respectively [33].

In nature gyrolite is a relatively rare mineral associated with hydrothermally changed basic rocks [34]. It occurs often in paragenesis with zeolites and other calcium silicate hydrates, such as okenite. Natural gyrolite has the general composition $(Na,Ca,Fe,\square)Ca_2[(Si,Al)_8O_{20}]_2[Si_8O_{20}][Ca_7(OH)_4]_2 \cdot 14H_2O$ with some variation in water content. Its structure was solved by Merlino [35] and comprises alternating octahedral and tetrahedral sheets. The Ca-octahedral sheets (O) are of portlandite type, i.e. with Ca–(O,OH) octahedra connected via sharing edges. These sheets are connected on both sides to two distinct types of silicate tetrahedral sheets via sharing oxygens. Both silicate sheets (S_1 and S_2) consist of Si-tetrahedra linked by sharing 3 oxygen atoms to form six-membered rings.

Alternating S_1–O–S_2 sheets are stacked along the *c* direction to form so-called "complex layers". These are linked together with additional cations in octahedral positions to build the so-called X-sheet. According to the proposed structure, the X-sheet consists of octahedral positions, which are up to 1/3 occupied. The resultant stacking sequence is approximately 22 Å.

Synthetic gyrolite was first prepared by Flint [36]. It can be readily obtained hydrothermally from mixtures of SiO_2

and CaO treated between 150 and 220 °C at C/S=2/3, yielding $Ca_2[Si_8O_{20}]_3[Ca_7(OH)_4]_2 \cdot 14H_2O$. At higher temperatures, a more highly polymerised phase (truscottite) occurs along with gyrolite [37,38]. Upon dehydration gyrolite begins to break down at about 630 °C, becomes amorphous, and at 860 °C transforms to wollastonite (α-wollastonite) and SiO_2 [39].

2. Experimental

2.1. Sample preparation

All samples were synthesised from CaO, ZnO (Merck), SiO_2 (highly dispersive, Merck) and H_2O with 0.1–10 wt.% Zn and w/s=20. CaO was freshly prepared from $CaCO_3$ (Merck) at 1000 °C for 24 h, and cooled under argon to avoid carbonation. Double-deionized water was decarbonated by boiling. All of the syntheses were performed under nitrogen atmosphere to avoid carbonation of the C-S-H phases via reactions with atmospheric carbon dioxide. A total of 12 precursor mixtures were prepared with target (Ca+Zn)/Si-molar ratios of 2/3 (0.66), and Zn/(Zn+Ca) molar ratios of 0, 1/400, 1/200, 1/100, 1/80, 1/50, 1/20, 1/15, 1/10, 1/8, 1/6 and 1/4.

The nanocrystalline phases were synthesised directly via mechanochemical synthesis [40,41] in an ordinary ball mill, whilst the crystalline phases required a second step, i.e. hydrothermal treatment, using the nanocrystalline phase as a precursor. The grinding time was fixed at 32 h, with grinding being stopped for 1 h every half an hour to minimise sample heating. Table 1 details the various samples.

The mechanochemically treated samples were then subdivided into two portions, the nanocrystalline phases and the portion requiring hydrothermal treatment. In the former case, the samples were dried at 60 °C under nitrogen.

Hydrothermal treatment was performed in Teflon-lined steel autoclaves at 210 °C for 96 h. The products were filtered, washed with double-distilled, decarbonated water and dried at 60 °C as above.

2.2. Sample characterisation

2.2.1. ESEM

Sample morphology was investigated using a Philips XL30-FEG Environmental Scanning Electron Microscope. The images were obtained using a gaseous secondary electron detector with water vapour as the imaging gas. Typical operating conditions were a water vapour partial pressure of 1.0 Torr and 15 kV accelerating voltage, although slight variations were occasionally used to optimise image quality. Semi-quantitative chemical analysis were performed at 20 kV via an energy dispersive detector (EDAX).

There was no need for sample treatment prior to imaging. Powder samples were simply sprinkled onto adhesive-backed carbon foils which were fixed to the sample holders and introduced into the microscope.

2.2.2. XRD

Powder X-ray diffraction, for determining cell parameters, was performed on silicon-doped (NIST640b) synthetic samples using a Bruker-AXS D5000 diffractometer employing Cu $K\alpha_{1,2}$ radiation and a graphite secondary monochromator. The cell parameters were determined using the Le Bail algorithm [42] in the software Topas v.2 [43]. The profile fitting was performed using the fundamental parameters approach [44]. Silicon was included in the refinement procedure, keeping its cell parameters equal to those of NIST SRM 640b (ICDD27-1402).

To ascertain the presence of amorphous content in our samples, 3 selected samples (0, 1/50, 1/15) were doped with 15 wt.% α-Al_2O_3 and measured in reflection mode using a D8 Advance diffractometer (Bruker-AXS) equipped with a CuKα anode and a Si(Li) solid-state energy dispersive detector. Measurements were performed over a 3–140° 2Θ range, with a 0.02° step size and 15 s/step. A set of variable divergent slits were used to maintain an illuminated sample length of 20 mm. Quantitative refinements with the Rietveld method were performed using TOPAS v.2 (Bruker AXS, 2000). The diffraction profiles were calculated using the fundamental parameters approach [44]. As a starting model

Table 1
Details of the samples investigated: NC=nanocrystalline, C=crystalline, X=unknown phase

(Ca+Zn)/Si	Zn/(Zn+Ca)	Sample	Phases	Sample	Phases
2/3	0	NC0.0	C-S-H(I)	C0.0	gyrolite
2/3	1/400	NC1.400	C-S-H(I)	C1.400	gyrolite
2/3	1/200	NC1.200	C-S-H(I)	C1.200	gyrolite
2/3	1/100	NC1.100	C-S-H(I)	C1.100	gyrolite
2/3	1/80	NC1.80	C-S-H(I)	C1.80	gyrolite
2/3	1/50	NC1.50	C-S-H(I)	C1.50	gyrolite
2/3	1/20	NC1.20	C-S-H(I)	C1.20	gyrolite
2/3	1/15	NC1.15	C-S-H(I)	C1.15	gyrolite
2/3	1/10	NC1.10	C-S-H(I)	C1.10	gyrolite
2/3	1/8	NC1.8	C-S-H(I)	C1.8	gyrolite
2/3	1/6	NC1.6	C-S-H(I)	C1.6	gyrolite
2/3	1/4	NC1.4	C-S-H(I)+zincite	C1.4	gyrolite+X

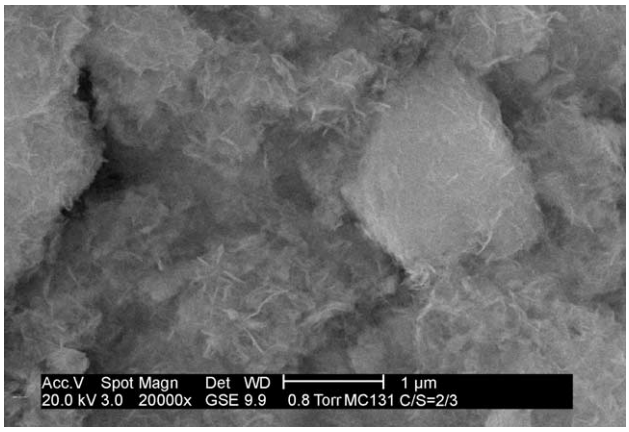

Fig. 1. ESEM image of nanocrystalline C-S-H (NC0.0), Zn/(Zn+Ca)=0.

we used the structures of gyrolite after Merlino (ICSD68199), corundum (ICSD31545) and low quartz (ICSD174). The structure of Merlino was modified slightly as follows. For all three samples, the occupation of the Na-position was set to zero and the Al contribution at position Si12 (sharing oxygen atoms with calcium from the X-sheet) was eliminated, leaving full Si occupancy of this position. In accordance with simulated powder diffraction patterns (vide infra), we set Zn^{2+} on the Ca8 position with occupancies of 0.16Zn:0.84Ca and 0.53Zn:0.47Ca to obtain Zn/(Zn+Ca) ratios of 1/50 and 1/15 for samples C1.50 and C1.15, respectively.

The zero point, sample displacement, cell parameters and crystal size of all the phases involved were refined. The preferred orientation of gyrolite was accounted for using sixth degree spherical harmonic functions. No preferred orientation was assumed for α-Al_2O_3 and quartz.

The quantitative analyses were conducted without further refinement of the atomic positions and temperature factors to keep the number of the variable parameters as low as possible.

2.2.3. X-ray photoelectron spectroscopy

Not all of the samples were analysed by XPS. Limitations regarding the sensitivity of the technique for zinc binding energies meant that only samples with Zn/(Zn+Ca)>1/20 were analysed.

Samples were analysed as received, the powders being pressed onto adhesive-backed copper tape before introduction into the vacuum chamber. Analysis was performed using a VG Escascope fitted with a MgKα ($h\nu$=1253.6 eV) X-ray source operating at 260 W (13 kV, 20 mA). After an initial wide spectrum, regional spectra were recorded with a 30 eV pass energy for the important elemental lines, (Si 2p, Ca 2p, Zn 2p and C 1s). Data were extracted from the spectra via peak fitting using XPSPeak software (available by download from: http://www.phy.cuhk.edu.hk/~surface/). A Shirley background and 80:20 Gaussian/Lorentzian peak shapes were assumed in all cases. Spectra were corrected for charging effects against the adventitious hydrocarbon peak at 284.8 eV.

2.2.4. Thermal analysis (DTA–TG)

DTA/TG measurements were performed on a SEIKO TA-Disk-Station with DTA/TG 320 module. Measurements were over the temperature range 60–930 °C, at a heating rate of 10 °C/min, under nitrogen flux. The samples were stored at 60 °C for at least 24 h before analysis.

3. Results and discussion

3.1. ESEM

The nanocrystalline samples comprised nearly spherical, compact aggregates, independent of Zn content (Figs. 1 and 2). The crystalline gyrolite samples showed changes in morphology depending upon zinc content. An absence of zinc led to crumpled foil formation (Fig. 3), whilst at higher contents, ball-shaped aggregates were formed (Fig. 4). The balls are composed of gyrolite panels. Additional phases were not identifiable.

EDX investigations of the crystalline and nanocrystalline phases showed Zn/(Zn+Ca) and (Ca+Zn)/Si ratios, corresponding to the reaction mixtures.

3.2. XRD

Mechanochemical synthesis yielded nanocrystalline Zn-substituted C-S-H phases. Fig. 5 shows XRD plots of nanocrystalline C-S-H phases ((Ca+Zn)/Si=2/3) with different zinc contents.

Standard diffraction patterns for tobermorite (ICDD83-1520) and C-S-H(I) (ICDD34-0002) were used to identify the nanocrystalline C-S-H phases. The samples with Zn/(Zn+Ca) ratios up to 1/6 showed the presence of C-S-H(I) and minor quantities of quartz. At Zn/(Zn+Ca)=1/4 zincite (ZnO) was also present. With increasing zinc content, there

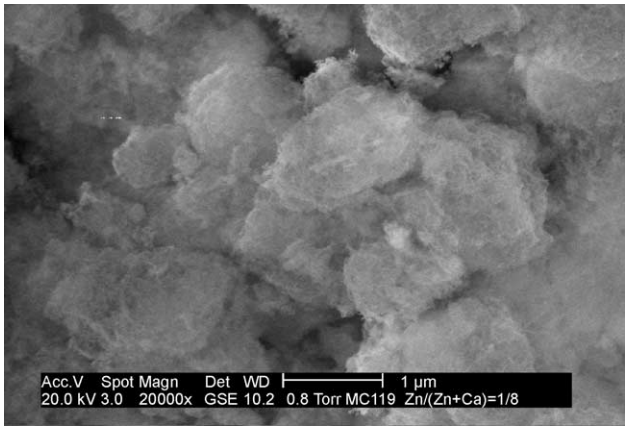

Fig. 2. ESEM image of nanocrystalline C-S-H (NC1.8), Zn/(Zn+Ca)=1/8.

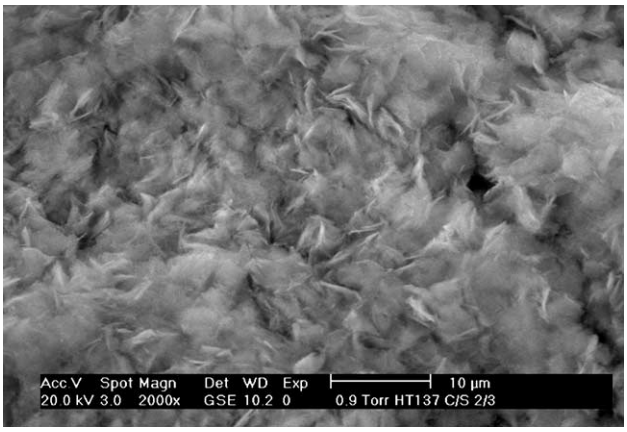

Fig. 3. ESEM image of crystalline gyrolite (C0.0), Zn/(Zn+Ca)=0.

was a decrease in the intensity of the basal reflection of C-S-H gel (C-S-H(I)).

Combined mechanochemical–hydrothermal synthesis led to gyrolite formation. All samples showed typical XRD patterns for gyrolite (Fig. 6) with quartz also being present at Zn/(Zn+Ca)>1/50. At Zn/(Zn+Ca)=1/4, there is a hump in the diffraction pattern at about 16 Å, which may be assigned to another zinc-rich phase, probably similar to minehilite $(K,Na)_2Ca_{28}Zn_5Al_4Si_{40}O_{112}(OH)_{16}$ [45]. As with the nanocrystalline phases, we observed a gradual decrease in the intensity of the reflection (001) (basal reflection) for the series. That both series behave similarly may be explained by assuming similar zinc incorporation mechanisms into both nanocrystalline and crystalline samples. The most probable mechanism seems to be incorporation in the interlayer of the C-S-H(I) [14] analogous to the tobermorite structure [46]. The X-sheet of gyrolite structure shows similarities to the Ca-interlayer in tobermorite. Therefore, we propose that the incorporation of Zn in gyrolite most probably takes place via substitution of Ca for Zn in the X-sheet. Interestingly, we observe that the uptake of Zn into both C-S-H(I) and

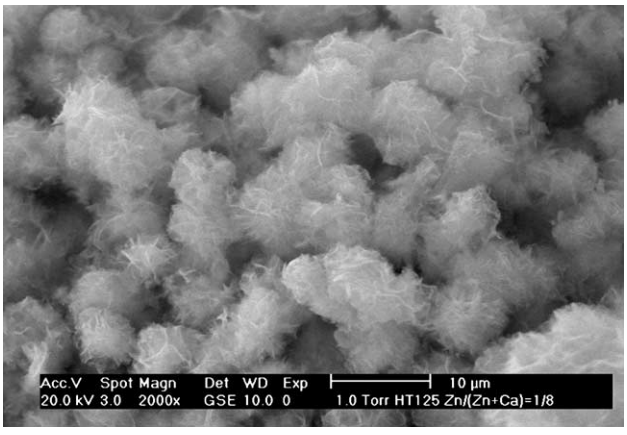

Fig. 4. ESEM image of crystalline gyrolite (C1.8), Zn/(Zn+Ca)=1/8.

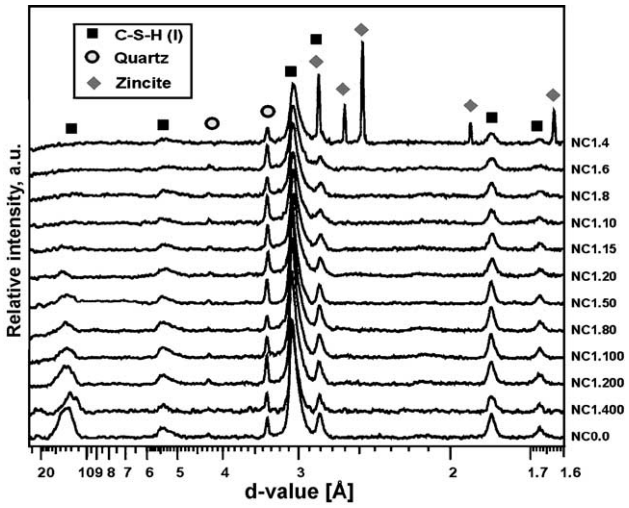

Fig. 5. XRD plots of zinc-substituted nanocrystalline C-S-H phases ((Ca+Zn)/Si=2/3).

gyrolite is possible to similar limits (up to Zn/(Zn+Ca)=1/6, corresponding to ca. 6 wt.% Zn). Once again, this may confirm the assumption of similar incorporation mechanisms in both sample series.

Profile fitting by the Le Bail method showed little change in the unit cell parameters of all the crystalline phases, except for the *c* parameter which shortened with increasing zinc content (Table 2). This can be interpreted as proof for zinc incorporation within the gyrolite structure.

Quantitative Rietveld refinements were performed on three selected samples, C1.200, C1.50 and C1.15, to estimate amorphous content in the hydrothermally treated samples. The first sample (C1.200) contained only gyrolite, whilst samples C1.50 and C1.15 also contained a small quantity of quartz (Table 3).

The quantitative analyses (Table 3) revealed negligible amorphous contents, Additionally, we observed quartz in samples C1.50 (about 1 wt.%) and C1.15 (about 3 wt.%).

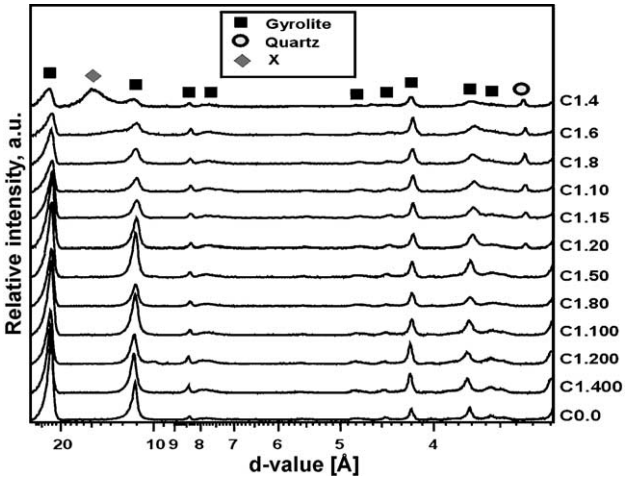

Fig. 6. XRD plots of zinc substituted crystalline C-S-H phases ((Ca+Zn)/Si=2/3).

Table 2
Cell parameters of gyrolite derived from the Le Bail method

	C0.0	C1.400	C1.200	C1.100	C1.80	C1.50	C1.20	C1.15	C1.10	C1.8	C1.6	C1.4
a (Å)	9.7290(8)	9.7324(4)	9.744(1)	9.741(16)	9.7389(8)	9.732(2)	9.7412(8)	9.7340(9)	9.7335(9)	9.7256(9)	9.728(2)	9.736(1)
b (Å)	9.7290(8)	9.7324(4)	9.744(1)	9.746(16)	9.7389(8)	9.732(2)	9.7412(8)	9.7340(9)	9.7335(9)	9.7256(9)	9.728(2)	9.736(1)
c (Å)	22.370(3)	22.391(2)	22.368(3)	22.332(25)	22.349(3)	22.350(3)	22.338(3)	22.295(3)	22.319(3)	22.3264(35)	22.266(6)	22.265(3)
α (°)	94.90(1)	95.810(4)	95.858(4)	95.81(8)	94.90(1)	95.82(1)	94.90(2)	94.92(2)	94.90(2)	94.96(2)	94.92(3)	94.80(1)
β (°)	92.13(1)	91.390(4)	91.362(4)	91.37(7)	92.06(1)	91.40(1)	92.27(2)	92.46(1)	92.49(2)	92.48(2)	92.49(3)	92.18(1)
γ (°)	120.00	120.00	120.00	120.00	120.00	120.00	120.00	120.00	120.00	120.00	120.00	120.00
V (Å^3)	1819.2(4)	1820.4(2)	1822.9(5)	1818(6)	1821.4(4)	1817(8)	1820.7(4)	1813.7(4)	1815.4(4)	1812.8(5)	1808.8(8)	1813.7(4)
R_{Bragg}	0.128	0.773	1.225	1.017	0.236	2.99	0.193	0.210	0.284	0.311	0.352	0.124
R_{exp}	6.256	6.35	6.465	3.97	6.613	3.90	6.259	6.627	6.347	6.150	6.077	5.830
R_{wp}	9.346	8.28	8.681	8.66	10.528	13.78	10.286	9.472	11.030	10.797	10.572	12.956
R_{p}	6.745	6.05	6.292	6.14	7.535	7.23	7.707	7.093	8.324	8.151	7.864	9.390
DWS	1.122	1.30	1.127	1.14	0.841	0.40	0.894	1.051	0.837	0.862	0.686	0.488
GOF	1.494	1.21	1.343	2.18	1.592	3.54	1.643	1.429	1.738	1.756	1.740	2.222

Table 3
Results from the quantitative Rietveld refinement of samples C1.200, C1.50 and C1.15

Sample	R values	Quantitative analysis [wt.%]
C1.200	R_{exp}: 3.16	Gyrolite 84.33(65)
	R_{wp}: 7.65	Corundum 15.67(65)
	R_p: 5.21	
	GOF: 2.42	
C1.50	R_{exp}: 3.13	Gyrolite 83.89(55)
	R_{wp}: 7.61	Corundum 15.17(51)
	R_p: 5.09	Quartz 0.94(13)
	GOF: 2.43	
C1.15	R_{exp}: 3.06	
	R_{wp}: 6.38	Gyrolite 81.90(15)
	R_p: 4.53	Corundum 15.10(14)
	GOF: 2.08	Quartz 2.96(27)

3.3. X-ray photoelectron spectroscopy (XPS)

Whilst many groups have used XPS for the study of cement systems [47–53], structural studies in this field are not too common [54–56]. Of particular relevance to this current study are those of [10,53], who observed reduced silicate polymerisation in zinc-doped Portland cement compared to non-doped cement.

3.3.1. Si 2p spectra

The Si 2p binding energies and peak widths for the various phases with increasing zinc content are shown in (Fig. 7). The crystalline phases have significantly higher binding energies than the nanocrystalline phases, but there was no dependence upon zinc content for either set of samples. The binding energies of the crystalline samples, at approximately 102.8 eV, are typical of phyllosilicates [54], whilst the nanocrystalline samples' lower binding energies imply less polymerisation. That zinc incorporation results in no changes in Si 2p binding energy is evidence that zinc replaces calcium and not silicon in the gyrolite structure, cf. aluminium substitution in 11 Å tobermorite, leading to a decrease in Si 2p binding energy [56].

Zinc incorporation led to Si 2p peak broadening. This implies greater variations in the bonding environments of silicon, due to the formation of Si–O–Zn bonds in addition to the Si–O–Si and Si–O–Ca bonds present in the pure systems, which confirms the XAFS data of [13].

3.3.2. Ca 2p spectra

The crystalline gyrolite samples all showed Ca $2p_{3/2}$ binding energies of approximately 347.5 eV. Those of the nanocrystalline samples were typically 0.3 eV lower and are similar to those reported for hydrated cement pastes [51,52]. C-S-H phyllosilicates have higher Ca 2p binding energies than either ino- or nesosilicates [54]. Thus, the crystalline gyrolite samples possess phyllosilicate structures, whilst the nanocrystalline samples are not as highly polymerised. If zinc incorporation was to cause severe silicate depolymerisation, then a marked decrease in Ca 2p binding energies would be observed, which was not the case.

3.3.3. Zn 2p spectra

Unfortunately, the quality of the Zn 2p spectra was such that very little useful information could be obtained from them. This was hindered further by the fact that the range in

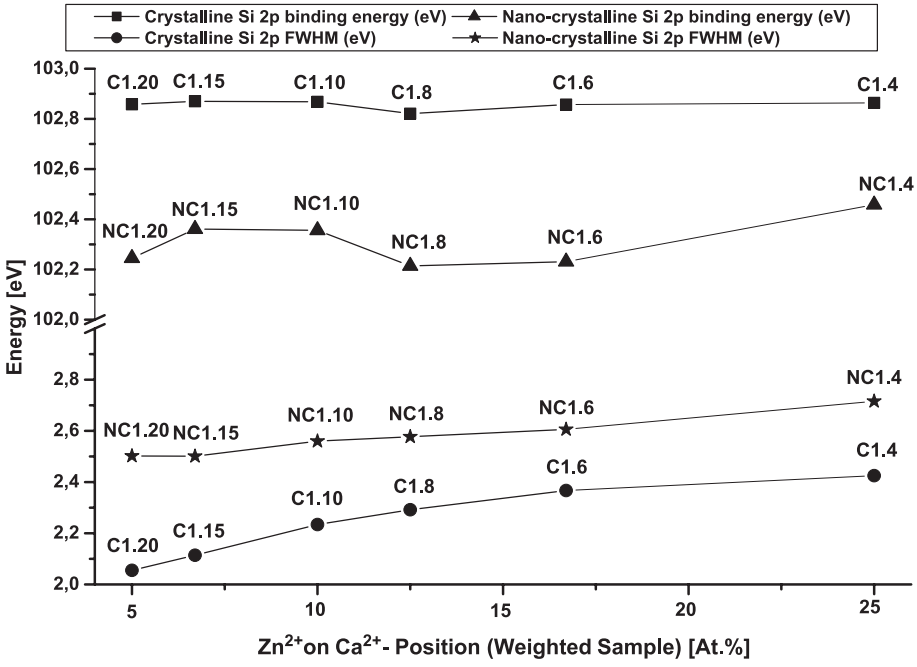

Fig. 7. Variation in Si 2p binding energies and peak widths (FWHM) with zinc content.

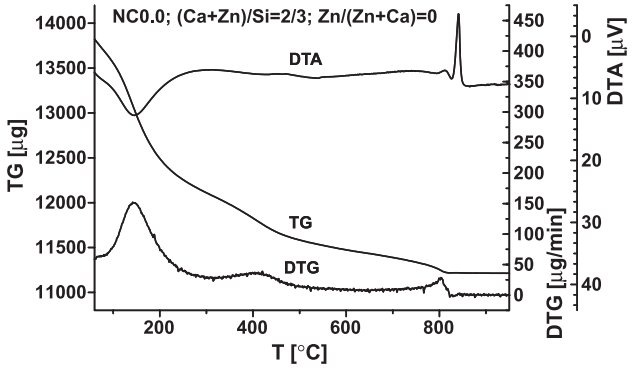

Fig. 8. DTA–TG plot of the nanocrystalline sample NC0.0.

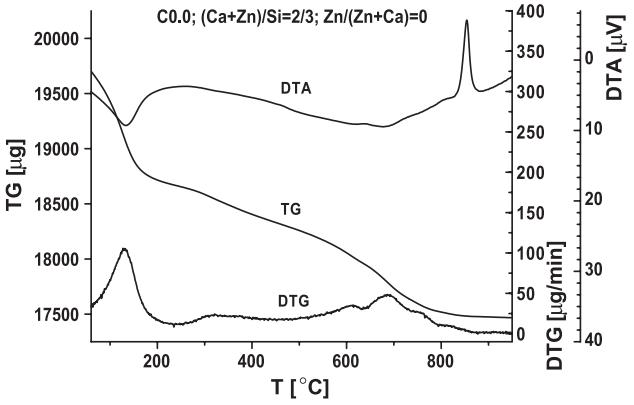

Fig. 10. DTA–TG plot of the crystalline sample C0.0.

Zn 2p binding energies is very small, rendering accurate identification difficult. Zinc could be detected at Zn/(Zn+Ca)>1/20, but the peak intensity was too small for accurate identification.

3.4. Thermogravimetry (TG)

The TG curves reveal a steady weight loss from 60 °C to 930 °C for all nanocrystalline samples (e.g. NC0.0, Fig. 8). The DTG curve shows the weight loss per unit time, this being a maximum for all nanocrystalline samples at approximately 150 °C.

There is a decrease in total weight loss with increasing zinc content from 19.8 wt.% to 15.2 wt.%. The thermogravimetry results for the nanocrystalline phases are shown in Fig. 9. The upper regression line shows the variation in total weight loss with zinc content, and the lower line shows weight loss up to 220 °C.

Both regression lines have approximately similar slopes. The weight losses between 220° and 930 °C, where chemically bound water and OH groups are lost, show similar values for all samples. Over the temperature range 60–220 °C, only molecular water is lost. It is this value which decreases with increasing zinc content. Thus the incorporation of zinc leads to decreasing water content.

The TG curves for the crystalline samples similarly show weight losses with increasing temperature as seen for the nanocrystalline samples. Fig. 10 shows, for example, the TG and DTG curves of sample C0.0. The DTG curves of the all crystalline samples show a maximum rate of weight loss at a temperature of approximately 130 °C, similar to the nanocrystalline samples. Fig. 11 indicates that the samples with Zn/(Zn+Ca)≤1/50 show a weight loss to 1000 °C close to (often slightly under) the theoretical value of 12.8 wt.%, calculated from the formula $Ca_{16}Si_{24}O_{60}(OH)_8 \cdot 14H_2O$. Samples with higher zinc contents showed lower weight losses. The top regression line in Fig. 11 shows the dependence of total weight loss with zinc content. Closer examination of the data shows that all samples exhibited an almost equal weight loss over the temperature range where molecular water is lost (up to 600°). All weight losses above 600 °C may be ascribed to OH groups. Thus the diminishing total weight loss with increasing zinc content may be

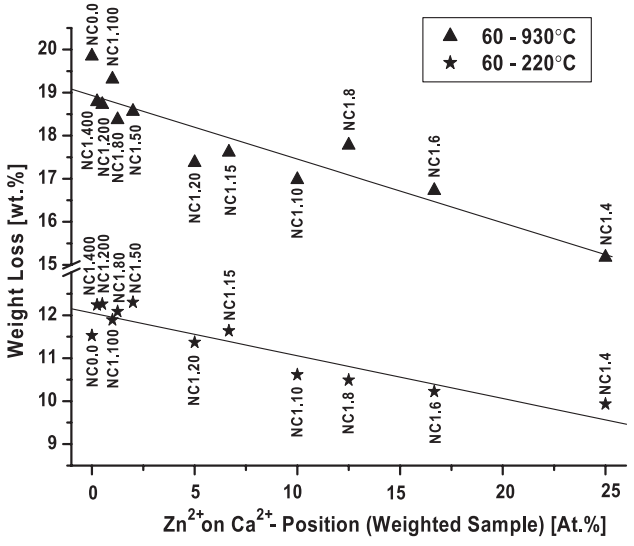

Fig. 9. Dependence of weight loss of the nanocrystalline phases, upon thermogravimetrical analysis, versus zinc content.

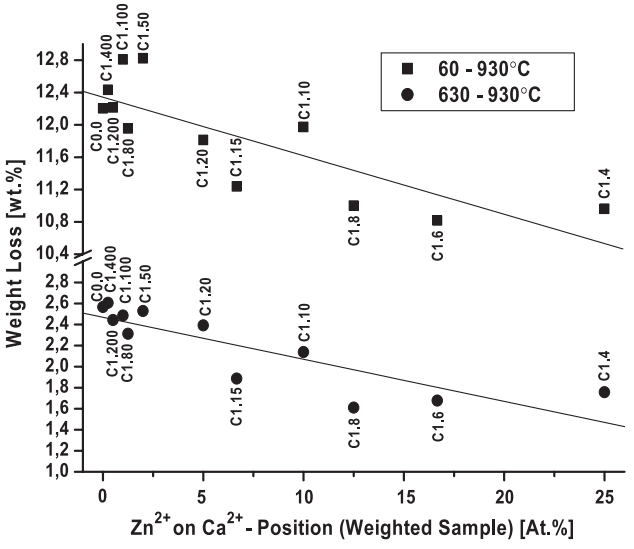

Fig. 11. Dependence of weight loss of the crystalline phases, upon thermogravimetrical analysis, versus zinc content.

ascribed to a decreasing OH content in the zinc-substituted gyrolite structure. In both regression lines, i.e. that for total weight loss and for weight loss over 630 °C have approximately similar slopes, again supporting our supposition. Up to sample C1.20, the weight loss over 630°C is 2.4–2.6 wt.%, corresponding to 7–8 OH groups. Samples with higher zinc contents show weight losses of 1.6–2.1 wt.%, roughly equivalent to 5–6 OH groups.

Thermogravimetric studies of natural and synthetic gyrolite show that, up to 400 °C, samples lose about 12 of 14 molecules of water [39]. The remaining 2 water molecules are still present up to 600 °C, probably due to particular dissociation to OH groups only.

3.5. Differential thermal analysis (DTA)

Examples of the endothermal and exothermal reactions, observed by differential thermal analysis, of the nanocrystalline and the crystalline samples are shown in Figs. 8 and 10, respectively.

The largest endothermal peak corresponds to the maximum rate of water loss in both groups of samples. The largest exothermal peak appears at approximately 830 °C (±20 °C) in both groups, characteristic of the formation temperature of wollastonite.

The nanocrystalline phases show a transformation temperature of 829 °C with no zinc (Fig. 12). Zinc contents up to 1/200 give rise to increasing transformation temperatures, up to 832 °C. Above these zinc contents, there is a decrease in transformation temperature with increasing zinc content. At (Zn/Zn+Ca)=1/4, the transformation temperature is as low as 811 °C.

The zinc-free crystalline phase shows a transformation temperature of 837 °C (Fig. 12). Analogous to the nanocrystalline samples, the transformation temperature initially increases with increasing zinc content (Fig. 12), to a maximum of 852 °C for Zn/(Zn+Ca)=1/50, then falling to 827 °C for the highest zinc content.

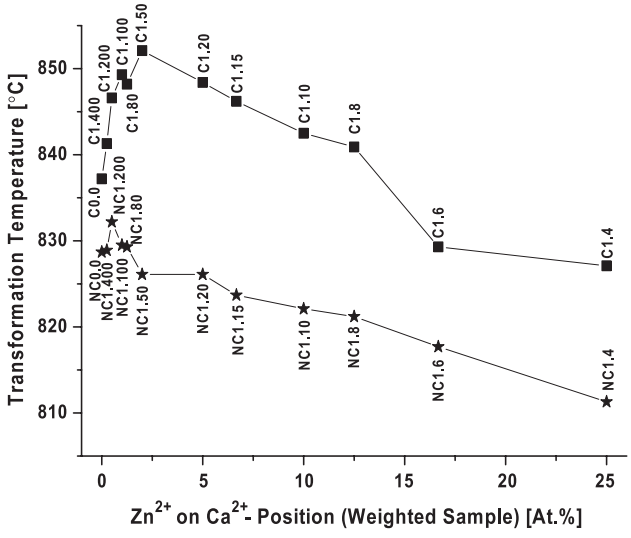

Fig. 12. Wollastonite onset temperature of the nanocrystalline and crystalline phases versus zinc content.

These results indicate increased thermal stability of the structures (NC; C) to certain zinc contents, above which additional zinc leads to destabilisation of the structure. The crystalline samples in average show higher transformation temperatures than the nanocrystalline samples. This may be explained by a lower degree of polymerisation in the nanocrystalline samples, in agreement with our XPS results.

4. Conclusions

1. Nanocrystalline phases, with C/S ratios of 2/3, may incorporate zinc up to a limit of Zn/(Zn+Ca)=1/6. At Zn/(Zn+Ca)≥1/4, zincite is also present. With increasing zinc content, a gradual decrease in the intensity of the basal reflection in the diffraction pattern occurs. Thus, zinc incorporation deteriorates the three-dimensional structural order of C-S-H(I).
2. Zinc incorporation into synthetic gyrolite is also possible up to Zn/(Zn+Ca)=1/6. Above this, i.e. Zn/(Zn+Ca)≥1/4, a hump is visible in the diffraction pattern at about 16 Å. This may be assigned to another zinc-rich phase, probably similar to minehilite. Thus both the nanocrystalline and the crystalline samples, with C/S=2/3, are able to incorporate zinc to a similar degree, i.e. Zn/(Zn+Ca)~1/6, corresponding to approximately 6 wt.%. Increasing zinc content led to a gradual diminishing of the basal reflection (001) of gyrolite, as for the nanocrystalline phases. This strongly supports the idea of similar incorporation mechanisms in both sample series. This appears to involve incorporation of Zn into the interlayer of the C-S-H(I) and X-sheet of gyrolite for nanocrystalline and crystalline samples, respectively.
3. Quantitative Rietveld analyses of selected crystalline samples, using external standards, showed that the gyrolite samples were free from amorphous content. This, together with the absence of zincite, is further proof for the incorporation of zinc into the gyrolite structure.
4. Shortening of the *c*-lattice parameter indicates incorporation of octahedrally coordinated zinc into the X-layer of gyrolite. Tetrahedral coordination can be excluded because it should cause a more substantial shortening of the lattice parameters.
5. Si 2p photoelectron spectra revealed the nanocrystalline phases to be less highly polymerised than the crystalline phases. Zinc incorporation did not lead to changes in Si 2p photoelectron binding energies, indicating Ca–Zn substitution.
6. With increasing zinc content, the zinc-substituted gyrolites showed decreasing weight loss due to dehydroxylation at temperatures above 630 °C. These samples also showed an increasing quartz content with increasing

zinc. Thus the samples became progressively enriched in Me^{2+} cations, (Ca+Zn)/Si rises and deprotonisation of the OH groups in the octahedral layer takes place to balance the overall charge.

7. The nanocrystalline samples comprised nearly spherical, compact aggregates, independent of zinc content. The crystalline samples exhibited a crumpled foil morphology at low zinc contents, whilst at higher contents, ball-shaped aggregates were formed.
8. The thermal stability of the structures in both groups of samples increases to a certain zinc content, above which additional zinc leads to a destabilisation of the structure.

Acknowledgements

The authors gratefully acknowledge the assistance of Dr. Keith Hallam and Professor Geoff Allen at the IAC, Bristol, England with the XPS measurements.

References

[1] F.P. Glasser, Fundamental aspects of cement solidification and stabilisation, J. Hazard. Mater. 52 (1997) 151–170.
[2] X. Zhang, W. Chang, T. Zhang, C.K. Ong, Nanostructure of calcium silicate hydrate gels in cement paste, J. Am. Ceram. Soc. 83 (10) (2000) 2600–2604.
[3] F.R.D. Andrade, V. Maringolo, Y. Kihara, Incorporation of V, Zn and Pb into the crystalline phases of Portland clinker, Cem. Concr. Res. 33 (2003) 63–71.
[4] H. Bolio-Arceo, F.P. Glasser, Zinc oxide in cement clinkering: Part I. Systems CaO–ZnO–Al_2O_3 and CaO–ZnO–Fe_2O_3, Adv. Cem. Res. 1 (10) (1998) 25–32.
[5] H.F.W. Taylor, Hydration of Portland cement, Cement Chemistry, Academic Press. Harcourt Brace Jovanovich Publishers, London San Diego New York Boston Sydney Tokyo Toronto, 1990, 199–242.
[6] I. Odler, O. Schmidt, Structure and properties of Portland cement clinker doped with zinc oxide, J. Am. Ceram. Soc. 60 (1980) 13–16.
[7] M. Murat, F. Sorrentino, Effect of large intakes of Cd, Pb, Cr, Zn to cement raw meal on the mineralogical composition of the clinker, in: L. Jany, A. Nisperos, J. Bayles (Eds.), Proceedings of the 18th International Conference on Cement Microscopy, Houston, Texas, April 21–25, 1996, pp. 272–279.
[8] H. Bolio-Arceo, F.P. Glasser, Zinc oxide in Portland cement: Part II. Hydration, strength gain and hydrate mineralogy, Adv. Cem. Res. 4 (12) (2000) 174–179.
[9] G. Arliguie, J. Grandet, Influence de la composition d'un ciment Portland sur son hydratation en presence de zinc, Cem. Concr. Res. 20 (1990) 517–524.
[10] M.Y.A. Mollah, T.R. Hess, Y.-N. Tsai, D.L. Cocke, An FTIR and XPS investigations of the effects of carbonation on the solidification/stabilization of cement based systems—Portland type V with zinc, Cem. Concr. Res. 23 (1993) 773–784.
[11] C.S. Poon, A.I. Clark, C.J. Peters, R. Perry, Mechanisms of metal fixation and leaching by cement based fixation processes, Waste Manage. Res. 3 (1985) 127–142.
[12] I. Moulin, W.E.E. Stone, J. Sanz, J.-I. Bottero, F. Mosnier, C. Haehnel, Lead and Zinc retention during hydration of tri-calcium silicate, a study by sorption isotherms and 29SiNMR spectroscopy, Langmuir 15 (1999) 2829–2835.
[13] F. Ziegler, A.M. Scheidegger, C.A. Johnson, R. Dähn, E. Wieland, Sorption mechanisms of zinc to calcium silicate hydrate: X-ray absorption fine structure (XAFS) investigation, Environ. Sci. Technol. 35 (2001) 1550–1555.
[14] F. Ziegler, R. Giere, C.A. Johnson, The sorption mechanisms of zinc to calcium silicate hydrate: sorption and microscopic investigations, Environ. Sci. Technol. 35 (2001) 4556–4561.
[15] W.L. Gong, L.M. Wang, R.C. Ewing, E. Vernaz, J.K. Bates, W.L. Ebert, Analytical electron microscopy study of surface layers formed on the French SON68 nuclear waste glass during vapour hydration at 200 °C, J. Nucl. Mater. 254 (1998) 249–265.
[16] E.S. Hodgkinson, C.R. Hughes, The mineralogy and geochemistry of cement/rock reactions: high resolution studies of experimental and analogue materials, in: R. Metcalfe, C.A. Rochelle (Eds.), Chemical Containment of Waste in the Geosphere, Special Publication Geological Society, London, 1999, pp. 195–211.
[17] H.F.W. Taylor, The calcium silicate hydrates, The Chemistry of Cements, Academic Press, London, 1964, pp. 167–232.
[18] H.F.W. Taylor, Cement Chemistry, Academic Press, Structural models for C-S-H gel, Harcourt Brace Jovanovich Publishers, London San Diego New York Boston Sydney Tokyo Toronto, 1990, 142–152.
[19] L.S. Dent-Glasser, E.E. Lachowski, K. Mohan, H.F.W. Taylor, A multi-method study of C_3S hydration, Cem. Concr. Res. 8 (1978) 733–739.
[20] E. Lippmaa, M. Magi, M. Tarmak, W. Wieker, A.-R. Grimmer, A high-resolution ^{29}Si NMR study of the hydration of tricalcium silicate, Cem. Concr. Res. 12 (1982) 597–602.
[21] I.G. Richardson, A.R. Brough, R. Brydson, G.W. Groves, C.M. Dobson, The location of aluminum in substituted calcium silicate hydrate (C-S-H) gels as determined by ^{29}Si and ^{27}Al NMR and EELS, J. Am. Ceram. Soc. 76 (1993) 2285–2288.
[22] I.G. Richardson, A.R. Brough, G.W. Groves, C.M. Dobson, The characterization of hardened alkali activated blast-furnace slag pastes and the nature of the calcium silicate hydrate (C-S-H) phase, Cem. Concr. Res. 24 (1994) 813–829.
[23] R.J. Kirkpatrick, J.L. Yarger, P.F. McMillan, P. Yu, X.D. Cong, Raman spectroscopy of C-S-H, tobermorite, and jennite, Adv. Cem. Based Mater. 5 (1997) 93–99.
[24] P. Yu, R.J. Kirkpatrick, B. Poe, P.F. McMillan, X. Cong, Structure of calcium silicate hydrate (C-S-H): near-, mid-, and far-infrared spectroscopy, J. Am. Ceram. Soc. 82 (3) (1999) 724–748.
[25] K. Fujii, W. Kondo, Estimation of thermochemical data for calcium silicate hydrate (C-S-H), J. Am. Ceram. Soc. 66 (12) (1983) 220–221.
[26] X.D. Cong, R.J. Kirkpatrick, ^{29}Si MASNMR study of the structure of calcium silicate hydrate, Adv. Cem. Based Mater. 3 (3/4) (1996) 144–156.
[27] I.G. Richardson, G.W. Groves, The microstructure and microanalysis of hardened cement pastes involving ground granulated blast-furnace slag, J. Mater. Sci. 27 (1992) 6204–6212.
[28] H.F.W. Taylor, Proposed structure for calcium silicate hydrate gel, J. Am. Ceram. Soc. 69 (1986) 464–467.
[29] H.F.W. Taylor, Tobermorite, jennite, and cement gel, Z. Kristallogr. 202 (1992) 41–50.
[30] R. Jauberthie, M. Temimi, M. Laquerbe, Hydrothermal transformation of tobermorite gel to 10 Å tobermorite, Cem. Concr. Res. 26 (1996) 1335–1339.
[31] J.A. Gard, T. Mitsuda, H.F.W. Taylor, Some observations on Assarsson's Z-phase and its structural relations to gyrolite, truscottite, and reyerite, Mineral. Mag. 40 (1975) 325–333.
[32] S. Shaw, C.M.B. Henderson, S.M. Clark, In-situ synchrotron study of the kinetics, thermodynamics, and reaction mechanisms of the hydrothermal crystallisation of gyrolite. $Ca_{16}Si_{24}O_{60}(OH)_8 \cdot 14H_2O$, Am. Mineral. 87 (2002) 533–541.
[33] Y. Okada, T. Masuda, H. Ishida, Behavior of silicate anions on the formation processes of gyrolite followed by -^{29}Si-NMR. Nippon Seramikkusu Kyokai Gakajutsu Ronbunshi, J. Ceram. Soc. Jpn. 103 (2) (1995) 124–127.

[34] A.L. Mackay, H.F.W. Taylor, Gyrolite, Mineral. Mag. 30 (1953) 80–91.
[35] S. Merlino, Gyrolite: its crystal structure and crystal chemistry, Mineral. Mag. 52 (1988) 377–387.
[36] E.P. Flint, H.F. McMurdie, L.S. Wells, Formation of hydrated calcium silicate at elevated temperatures and pressures, J. Res. Natl. Bur. Stand. 21 (1938) 617–638.
[37] K. Luke, H.F.W. Taylor, G.L. Kalousek, Some factors affecting formation of truscottite and xonotlite at 300–350 °C, Cem. Concr. Res. 11 (2) (1981) 197–203.
[38] K. Luke, H.F.W. Taylor, Equilibria and non-equilibria in the formation of xonotlite and truscottite, Cem. Concr. Res. 14 (5) (1984) 657–662.
[39] S. Shaw, Hydrothermal formation and high temperature dehydration of calcium silicate hydrate (C-S-H) phases: an in situ synchrotron study, PhD thesis, University of Manchester, 1999.
[40] K. Sasaki, T. Masuda, H. Ishida, T. Mitsuda, Synthesis of calcium silicate hydrate with Ca/Si=2 by mechanochemical treatment, J. Am. Ceram. Soc. 80 (1996) 472–476.
[41] F. Saito, G. Mi, M. Hanada, Mechanochemical synthesis of hydrated calcium silicates by room temperature grinding, Solid State Ionics 101–103 (1997) 37–43.
[42] A. Le Bail, H. Duroy, J.L. Fourquet, Ab initio structure determination of LiSBWO6 by X-ray-powder diffraction, Mater. Res. Bull. 23 (3) (1988) 447–452.
[43] Bruker AXS, TOPAS V2.0, General profile and structure analysis software for powder diffraction data, User Manual, Bruker AXS, Karlsruhe, Germany, 2000.
[44] R.W. Cheary, A.A. Coelho, A fundamental parameters approach of X-ray line-profile fitting, J. Appl. Crystallogr. 25 (1992) 109–121.
[45] Y. Dai, J.E. Post, D.E. Appleman, Crystal structure of minehillite: twinning and structural relationships to reyerite, Am. Mineral. 80 (1995) 173–178.
[46] S. Merlino, E. Bonaccorsi, T. Armbruster, The real structure of tobermorite 11Å: normal and anomalous forms, OD character and polytypic modifications, Eur. J. Mineral. 13 (2001) 577–590.
[47] S. Long, C. Liu, Y. Wu, ESCA study on the early C_3S hydration in NaOH solution and pure water, Cem. Concr. Res. 28 (2) (1998) 245–249.
[48] D. Ménétrier, I. Jawed, T.S. Sun, J. Skalny, ESCA and SEM studies on early C3S hydration, Cem. Concr. Res. 9 (1979) 473–482.
[49] M. Regourd, J.H. Thomassin, P. Baillif, J.C. Touray, Study of the early hydration of Ca_3SiO_5 by X-ray photoelectron spectrometry, Cem. Concr. Res. 10 (1980) 223–230.
[50] J.H. Thomassin, M. Regourd, P. Baillif, J.C. Touray, Étude de l'hydratation initiale du silicate bicalcique β par spectrométrie de photo-électrons, C. R. Acad. Sci. Paris 290 (1980 (Jan.)) 1–3.
[51] H.G. McWhinney, D.L. Cocke, K. Balke, J.D. Ortego, An investigation of mercury solidification and stabilization in Portland cement using X-ray photoelectron spectroscopy and energy dispersive spectroscopy, Cem. Concr. Res. 20 (1990) 79–91.
[52] D.L. Cocke, H.G. McWhinney, D.C. Dufner, B. Horrell, An XPS and EDS investigation of cement doped with Pb^{2+} and Cr^{3+} cations, Hazard. Waste Hazard. Mater. 6 (3) (1989) 251–267.
[53] D.L. Cocke, M.Y.A. Mollah, J.R. Parga, T.R. Hess, J.D. Ortego, An XPS and SEM/EDS characterization of leaching effects on lead- and zinc-doped Portland cement, J. Hazard. Mater. 30 (1992) 83–95.
[54] L. Black, K. Garbev, P. Stemmermann, K.R. Hallam, G.C. Allen, Characterisation of crystalline C-S-H phases by X-ray photoelectron spectroscopy (XPS), Cem. Concr. Res. 33 (6) (2003) 899–911.
[55] L. Black, A. Stumm, K. Garbev, P. Stemmermann, K.R. Hallam, G.C. Allen, X-ray photoelectron analysis of cement clinker phases, Cem. Concr. Res. 33 (10) (2003) 1561–1565.
[56] L. Black, A. Stumm, K. Garbev, P. Stemmermann, K.R. Hallam, G.C. Allen, X-ray photoelectron spectroscopy of aluminium-substituted tobermorite, Cem. Concr. Res. (in press available online 17 November 2004).